

Sharp Interface LES of Breaking Waves by an Interface Piercing Body in Orthogonal Curvilinear Coordinates

Zhaoyuan Wang¹, Jungsoo Suh², Jianming Yang³, Frederick Stern⁴

IIHR-Hydroscience and Engineering, University of Iowa, Iowa City, IA, 52242-1585, USA

A sharp interface LES methodology on orthogonal curvilinear grid for breaking waves produced by an interface-piercing body at high Reynolds number is presented. Both gas and liquid phases are considered for the strong interactions between two phases, such as spray dispersion and bubble entrainment. The level-set based ghost fluid method is adopted for sharp interface treatment and a volume-of-fluid method in orthogonal curvilinear coordinates is coupled with the level set method for enhanced interface tracking. A Lagrangian dynamic Smagorinsky subgrid-scale model is used for the spatially filtered turbulence closure. Several numerical tests are conducted in order to validate the code. Wave breaking around a wedge-shaped bow is simulated with the results compared with the experimental measurement.

I. Introduction

NUMERICAL simulation of ship flows is difficult and challenging since it involves two-phase interfacial flows interacting with moving bodies of complex geometries. In the study¹ by Yang and Stern, a sharp interface Cartesian grid solver (CFDSHIP-Iowa Version 6.1) was developed for the high-performance, high-fidelity, multi-scale simulation of two-phase turbulent flows in ship hydrodynamics. It is a very accurate, efficient and robust CFD tool with high order numerical schemes, simple code modules and structures, and little memory and CPU intensive. The techniques and schemes used in this solver have been extensively verified and validated and applied in the simulations related to ship hydrodynamics.¹⁻⁸ Cartesian grid is simple and easy to generate, and the complex geometry can be handled using the immersed boundary method (IBM). However, large numbers of grid points are required in order to resolve the boundary layer since the Cartesian grid line usually does not coincide with the body surface. For the curvilinear grid, grid refinement near the body surface can be easily achieved without significantly increasing the total grid points. For general curvilinear grid, the equation discretization and numerical procedures are usually complicated. This can be greatly simplified when an orthogonal curvilinear grid is used. The orthogonal curvilinear grid not only relaxes the limitations of the Cartesian grid but also retains the similar accuracy, robustness and efficiency as the Cartesian grid method, which is very useful for two-phase flow problems with simple geometries such as bump, cylinder, hydrofoil, wedge, etc. Herein, the Cartesian grid solver (Version 6.1) is extended to orthogonal curvilinear coordinates (Version 6.2) for fully resolved boundary layer as the first step towards a general curvilinear grid solver (Version 6.3). An effort of combining the Cartesian and orthogonal curvilinear grid solvers using an overset method (Version 6.2.5) was performed in Ref. 9.

In this paper, a sharp interface large-eddy simulation (LES) methodology on orthogonal curvilinear coordinates for the breaking waves produced by an interface-piercing body at high Reynolds numbers is presented. Both gas and liquid phases are considered for the strong interactions between two phases, such as spray dispersion and bubble entrainment. The level-set based ghost fluid method is adopted for sharp interface treatment and a volume-of-fluid method in orthogonal curvilinear coordinates is coupled with the level set method for enhanced interface tracking properties. A Lagrangian dynamic Smagorinsky subgrid-scale model is used for the spatially filtered turbulence closure. The orthogonal curvilinear grid solver is first tested by the LES predictions for fully-developed turbulent channel flow without considering two-phase effect. Several small-scale cases, bubbles and droplets, are calculated and compared with reference data to validate the sharp interface model on the orthogonal curvilinear grid. Finally, wave breaking around a wedge-shaped bow is simulated.

¹ Assistant Research Scientist, AIAA Member.

² Senior Researcher, AIAA Member.

³ Associated Research Scientist, AIAA Member.

⁴ Professor of Mechanical Engineering.

II. Mathematical Model and Numerical Methods

The mathematical model and numerical method in the orthogonal curvilinear coordinates used in this study are the extension of CFDShip-Iowa Version 6, a sharp interface Cartesian grid solver for two-phase incompressible flows recently developed at IIHR.¹ In this solver, the interface is tracked by a coupled level set and volume-of-fluid (CLSVOF) method.² A ghost fluid methodology is adopted to handle the jump conditions across the interface, where the density and surface tension effect are treated in a sharp way while the viscosity is smeared by a smoothed Heaviside function.

A. Navier-Stokes Equations and LES Modeling

For the incompressible turbulent flows of two immiscible fluids, e.g., air and water, the filtered Navier-Stokes equations written in the vector form are given as follows:

$$\frac{\partial \bar{\mathbf{u}}}{\partial t} + \bar{\mathbf{u}} \cdot \nabla \bar{\mathbf{u}} = -\frac{1}{\rho} \nabla \bar{p} - \nabla \cdot \bar{\boldsymbol{\tau}} + \frac{1}{\rho} \nabla \cdot \bar{\mathbf{T}} + \mathbf{g}, \quad (1)$$

$$\nabla \cdot \bar{\mathbf{u}} = 0, \quad (2)$$

where \bar{f} denotes the filter operation on a variable f , t is time, \mathbf{u} is the velocity vector, p is pressure, ρ is the density, \mathbf{g} represents the gravity acceleration, and \mathbf{T} is the viscous stress tensor defined as

$$\mathbf{T} = 2\mu\mathbf{S}, \quad (3)$$

with μ the dynamic viscosity and \mathbf{S} the strain rate

$$\mathbf{S} = \frac{1}{2}(\nabla \mathbf{u} + (\nabla \mathbf{u})^T). \quad (4)$$

$\bar{\boldsymbol{\tau}}$ is the subgrid-scale (SGS) stress tensor for the LES. In the LES, the small dissipative eddies are modeled by the SGS model whereas the large, energy carrying, eddies are resolved by the spatially filtered Navier-Stokes equations.

Since the fluid properties are discontinuous across the interface, which is a function of time and space, density and viscosity are also functions of time and space and only known with given interface position. They will be defined using the level set function later.

With the contravariant velocity components U_i ($i=1, 2, 3$), defined in the coordinates direction, chosen as the dependent variables, the Navier-Stokes equations can be fully transformed from the Cartesian coordinates (x, y, z) to the orthogonal curvilinear coordinates (x_1, x_2, x_3) :

$$\begin{aligned} \frac{\partial U_1}{\partial t} + \frac{1}{h_1 h_2 h_3} \frac{\partial}{\partial x_1} [h_2 h_3 (U_1 U_1 - \tau_{11})] + \frac{1}{h_1 h_2 h_3} \frac{\partial}{\partial x_2} [h_1 h_3 (U_1 U_2 - \tau_{12})] + \frac{1}{h_1 h_2 h_3} \frac{\partial}{\partial x_3} [h_1 h_2 (U_1 U_3 - \tau_{13})] = \\ - \frac{1}{\rho} \frac{1}{h_1} \frac{\partial p}{\partial x_1} + \frac{1}{h_1 h_2} \frac{\partial h_2}{\partial x_1} (U_2 U_2 - \tau_{22}) + \frac{1}{h_1 h_3} \frac{\partial h_3}{\partial x_1} (U_3 U_3 - \tau_{33}) - \frac{1}{h_1 h_2} \frac{\partial h_1}{\partial x_2} (U_1 U_2 - \tau_{12}) - \frac{1}{h_1 h_3} \frac{\partial h_1}{\partial x_3} (U_1 U_3 - \tau_{13}) \end{aligned}, \quad (5)$$

$$\begin{aligned} \frac{\partial U_2}{\partial t} + \frac{1}{h_1 h_2 h_3} \frac{\partial}{\partial x_1} [h_2 h_3 (U_1 U_2 - \tau_{12})] + \frac{1}{h_1 h_2 h_3} \frac{\partial}{\partial x_2} [h_1 h_3 (U_2 U_2 - \tau_{22})] + \frac{1}{h_1 h_2 h_3} \frac{\partial}{\partial x_3} [h_1 h_2 (U_2 U_3 - \tau_{23})] = \\ - \frac{1}{\rho} \frac{1}{h_2} \frac{\partial p}{\partial x_2} + \frac{1}{h_1 h_2} \frac{\partial h_1}{\partial x_2} (U_1 U_1 - \tau_{11}) + \frac{1}{h_2 h_3} \frac{\partial h_3}{\partial x_2} (U_3 U_3 - \tau_{33}) - \frac{1}{h_2 h_1} \frac{\partial h_2}{\partial x_1} (U_1 U_2 - \tau_{12}) - \frac{1}{h_2 h_3} \frac{\partial h_2}{\partial x_3} (U_2 U_3 - \tau_{23}) \end{aligned}, \quad (6)$$

$$\begin{aligned} \frac{\partial U_3}{\partial t} + \frac{1}{h_1 h_2 h_3} \frac{\partial}{\partial x_1} [h_2 h_3 (U_1 U_3 - \tau_{13})] + \frac{1}{h_1 h_2 h_3} \frac{\partial}{\partial x_2} [h_1 h_3 (U_2 U_3 - \tau_{23})] + \frac{1}{h_1 h_2 h_3} \frac{\partial}{\partial x_3} [h_1 h_2 (U_3 U_3 - \tau_{33})] = \\ - \frac{1}{\rho} \frac{1}{h_3} \frac{\partial p}{\partial x_3} + \frac{1}{h_1 h_3} \frac{\partial h_1}{\partial x_3} (U_1 U_1 - \tau_{11}) + \frac{1}{h_2 h_3} \frac{\partial h_2}{\partial x_3} (U_2 U_2 - \tau_{22}) - \frac{1}{h_3 h_1} \frac{\partial h_3}{\partial x_1} (U_1 U_3 - \tau_{13}) - \frac{1}{h_2 h_3} \frac{\partial h_3}{\partial x_2} (U_2 U_3 - \tau_{23}) \end{aligned}, \quad (7)$$

and

$$\frac{\partial}{\partial x_1} (h_2 h_3 U_1) + \frac{\partial}{\partial x_2} (h_1 h_3 U_2) + \frac{\partial}{\partial x_3} (h_1 h_2 U_3) = 0, \quad (8)$$

where

$$\tau_{11} = \nu_{eff} \left(\frac{2}{h_1} \frac{\partial U_1}{\partial x_1} + 2U_2 \frac{1}{h_1 h_2} \frac{\partial h_1}{\partial x_2} + 2U_3 \frac{1}{h_1 h_3} \frac{\partial h_1}{\partial x_3} \right), \quad (9)$$

$$\tau_{22} = \nu_{eff} \left(\frac{2}{h_2} \frac{\partial U_2}{\partial x_2} + 2U_1 \frac{1}{h_1 h_2} \frac{\partial h_2}{\partial x_1} + 2U_3 \frac{1}{h_1 h_3} \frac{\partial h_2}{\partial x_3} \right), \quad (10)$$

$$\tau_{33} = \nu_{eff} \left(\frac{2}{h_3} \frac{\partial U_3}{\partial x_3} + 2U_1 \frac{1}{h_1 h_3} \frac{\partial h_3}{\partial x_1} + 2U_2 \frac{1}{h_2 h_3} \frac{\partial h_3}{\partial x_2} \right), \quad (11)$$

$$\tau_{12} = \nu_{eff} \left(\frac{1}{h_2} \frac{\partial U_1}{\partial x_2} + \frac{1}{h_1} \frac{\partial U_2}{\partial x_1} - U_1 \frac{1}{h_1 h_2} \frac{\partial h_1}{\partial x_2} - U_2 \frac{1}{h_1 h_2} \frac{\partial h_2}{\partial x_1} \right), \quad (12)$$

$$\tau_{13} = \nu_{eff} \left(\frac{1}{h_3} \frac{\partial U_1}{\partial x_3} + \frac{1}{h_1} \frac{\partial U_3}{\partial x_1} - U_1 \frac{1}{h_1 h_3} \frac{\partial h_1}{\partial x_3} - U_3 \frac{1}{h_1 h_3} \frac{\partial h_3}{\partial x_1} \right), \quad (13)$$

$$\tau_{23} = \nu_{eff} \left(\frac{1}{h_2} \frac{\partial U_3}{\partial x_2} + \frac{1}{h_3} \frac{\partial U_2}{\partial x_3} - U_3 \frac{1}{h_2 h_3} \frac{\partial h_3}{\partial x_2} - U_2 \frac{1}{h_2 h_3} \frac{\partial h_2}{\partial x_3} \right). \quad (14)$$

The metric coefficients h_1, h_2, h_3 are defined by

$$h_i^2 = \left(\frac{\partial x}{\partial x_i} \right)^2 + \left(\frac{\partial y}{\partial x_i} \right)^2 + \left(\frac{\partial z}{\partial x_i} \right)^2, \quad i = 1, 2, 3. \quad (15)$$

The effective total viscosity is defined as $\nu_{eff} = \mu / \rho + \nu_t$ with ν_t the turbulent eddy viscosity.

B. Interface Modeling

Defining the interface Γ as the zero level set of a signed distance function ϕ , or the level set function, the position of the interface can be tracked by solving the level set evolution equation

$$\frac{\partial \phi}{\partial t} + \mathbf{u} \cdot \nabla \phi = 0. \quad (16)$$

In the coupled level set and volume-of-fluid method, the volume-of-fluid function, F , is defined as the liquid volume fraction in a cell with its value in between zero and one in a surface cell and zero and one in air and liquid respectively. The advection equation of F is

$$\frac{\partial F}{\partial t} + \mathbf{u} \cdot \nabla F = 0. \quad (17)$$

The level set function is corrected based on the reconstructed interface using VOF function for mass conservation.

With the level set function defined, the fluid properties, such as density and viscosity, are given by the following equations:

$$\begin{aligned} \rho &= \rho_G + (\rho_L - \rho_G)H(\phi) \\ \mu &= \mu_G + (\mu_L - \mu_G)H_\epsilon(\phi) \end{aligned} \quad (18)$$

where the subscripts G and L represent gas and liquid phase, respectively. $H(\phi)$ and $H_\epsilon(\phi)$ are the stepwise and smoothed Heaviside functions,¹ respectively.

As for the jump conditions at the interface, the velocity across the interface Γ is continuous, as the fluids are viscous and no phase change is considered here:

$$[\mathbf{u}] = 0, \quad (19)$$

and the jump condition for stress is

$$\left[\mathbf{n} \cdot \left(-p\mathbf{I} + \mu \left(\nabla \mathbf{u} + (\nabla \mathbf{u})^T \right) \right) \cdot \mathbf{n} \right] = \sigma \kappa, \quad (20)$$

where $[]$ indicates the jump at the interface, i.e., $f_L^I - f_G^I$ for a variable f with superscript I denotes interface, \mathbf{n} is the unit vector normal to the interface, σ is the coefficient of surface tension, and κ is the local curvature of the interface. Notice that with a continuous viscosity and velocity field, the stress jump condition Eq. (20) reduces to

$$[p] = p'_L - p'_G = -\sigma\kappa. \quad (21)$$

The level set and VOF advection Eqs. (16) and (17) can be rewritten in the orthogonal curvilinear coordinates (x_1, x_2, x_3) as,

$$\frac{\partial\phi}{\partial t} + U_1 \frac{\partial\phi}{h_1\partial x_1} + U_2 \frac{\partial\phi}{h_2\partial x_2} + U_3 \frac{\partial\phi}{h_3\partial x_3} = 0, \quad (22)$$

and

$$\frac{\partial F}{\partial t} + U_1 \frac{\partial F}{h_1\partial x_1} + U_2 \frac{\partial F}{h_2\partial x_2} + U_3 \frac{\partial F}{h_3\partial x_3} = 0, \quad (23)$$

respectively.

C. Numerical Methods and High Performance Computing

A finite-difference method is used to discretize the governing equations on a non-uniform staggered orthogonal grid, in which the contravariant velocity components (U_1, U_2, U_3) are defined at the cell face centers in the coordinates (x_1, x_2, x_3) directions, respectively. All other variables are defined at the cell centers. Time advancement of the present study is based on the semi-implicit four-step fractional step method.¹⁰ The diagonal diffusion terms are advanced with the second-order Crank–Nicholson method and the other terms by the second-order explicit Adams–Bashforth method. The pressure Poisson equation is solved to enforce the continuity equation.

The convective terms are discretized using the fifth-order Hamilton–Jacobi Weighted-ENO (HJ-WENO) scheme.¹¹ The other terms are discretized by the second-order central difference scheme. The pressure Poisson equation is solved using a semi-coarsening multigrid solver from the HYPRE library.¹² In general, the Poisson solver is the most expensive part of the whole algorithm and uses about 80–85% of the total computation time.

The level-set equations are solved using the third-order TVD Runge–Kutta scheme¹³ for time advancement and the fifth-order HJ-WENO scheme¹¹ for spatial discretization. These equations are solved for the cells in a narrow band about a few grid-cell width to reduce computational overhead.¹⁴ In the CLSVOF method, the interface is reconstructed via a PLIC scheme and the level set function is re-distanced based on the reconstructed interface. The interface is advected using a Lagrangian method with a second-order Runge–Kutta scheme for time integration.

The code is parallelized via a domain decomposition (in three directions) technique using the MPI library. All inter-processor communications for ghost cell information exchange are in non-blocking mode. In general, optimal load balance can be achieved except for a small amount of overhead due to interface, which may be unevenly distributed over processors. Parallel I/O using MPI2 have been implemented such that all processors read from and write to one single file simultaneously, which is much more effective than one or a few processors receive data from all processors and write to one or a few files and more convenient than every processor writes its own data files.

III. Results

In this section, the computational results of some numerical examples are presented. In the first example, the LES of a fully-developed turbulent channel flow is performed, in which only single phase flow is considered. The sharp interface method are validated using a small scale droplet and air bubble. Wave breaking by a wedge-shaped bow is chosen as an application example for the interface piercing body problems. Applications in the cylinder and bump flows have been reported in Refs. 15 and 16, respectively.

A. Channel Flow

LES predictions are obtained for fully-developed turbulent channel flow with a Reynolds number based on the bulk velocity, U_b , and channel half-height δ of 2800. The same non-dimensional computational domain size as the $Re_\tau = 180$ DNS case of Ref. 17 was used. A constant mesh spacing is used in the x and y directions. A non-uniform mesh spacing is used in the z direction using a *cosine* function. Periodic boundary conditions are enforced for all variables in the streamwise and spanwise directions. An artificial forcing mechanism suggested in Ref. 18 was used to mimic an imposed streamwise pressure gradient and to maintain a fixed mass flow rate. A Poiseuille parabolic streamwise velocity profile is used to initialize the streamwise velocity and random velocity fluctuations were superimposed on all three velocity components. The maximum CFL number is about 1. Figure 1 shows the time-averaged streamwise velocity profile, normalized by the friction velocity, on a logarithmic axis. The figure shows good agreement between the present LES results and the previous DNS results,¹⁷ especially in the viscous sub-layer and logarithmic region. There is a slight over-prediction of about 1.5 % near the centerline. This is most likely

caused by the enhanced dissipation leading to an under-prediction of the skin friction velocity due to the combined influences of the subgrid-scale model. The r.m.s. (root mean square) values for all three velocity components, normalized by friction velocity, are shown in Fig. 2 along with the DNS results.¹⁷ The profile of streamwise velocity fluctuations case is in very good agreement with the DNS results. The location and value of the peak are also well predicted. The spanwise and wall-normal velocity fluctuations are also in good agreement with the DNS data.

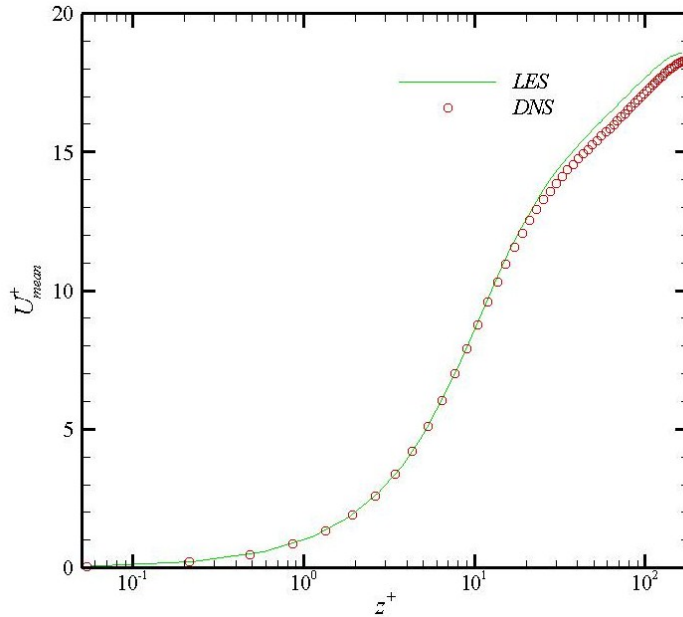


Figure 1. Mean streamwise velocity profiles for the channel flow case; logarithmic plot showing comparison to previous DNS data.¹⁷

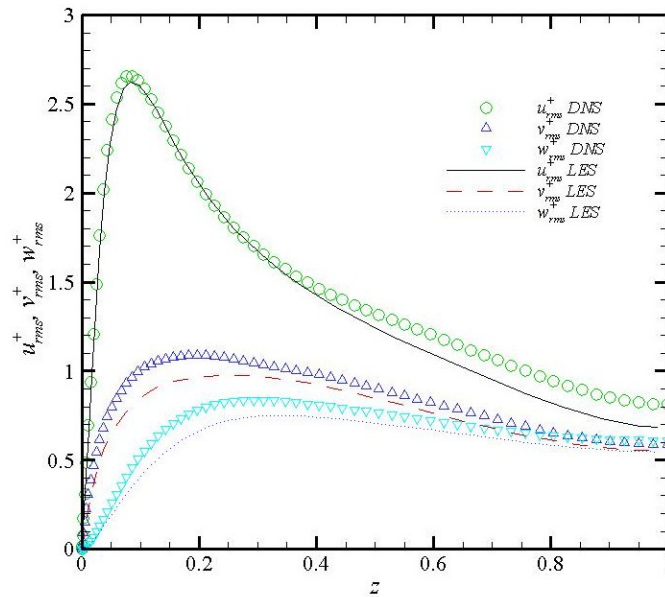


Figure 2. Streamwise, transverse, and spanwise velocity fluctuations for the channel flow case; comparison to previous DNS data.¹⁷

B. Air Bubble Rising in Quiescent Water

An air bubble with a diameter of 2 mm rising in quiescent water is simulated. Constant physical properties of air and water are chosen as: $\sigma = 0.0728 \text{ kg/s}^2$, $\rho_l = 1000 \text{ kg/m}^3$, $\rho_g = 1.226 \text{ kg/m}^3$, $\mu_l = 1.137 \times 10^{-3} \text{ kg/ms}$, $\mu_g = 1.78 \times 10^{-5} \text{ kg/ms}$, and the gravity $g = -9.8 \text{ m/s}^2$. The computations are conducted on an *annular sector* domain as shown in Fig. 3 with a grid size of $100 \times 100 \times 100$.

Figure 3 shows the bubble shapes at different time instants. For small size air bubbles, surface tension force is dominant and air bubbles can reach a steady state with a stable shape and constant rising velocity. As show in the figure, the predicted bubble shape is elliptical which is consistent with the experimental observations.¹⁹ The computed terminal velocity is 0.291mm/ms which is in excellent agreement with the experimental value of 0.287 mm/ms calculated using the experimental correlation proposed in Ref. 20, which is given by

$$u_T = \sqrt{2\sigma / \rho_l d_e + \Delta\rho g d_e / 2} . \quad (24)$$

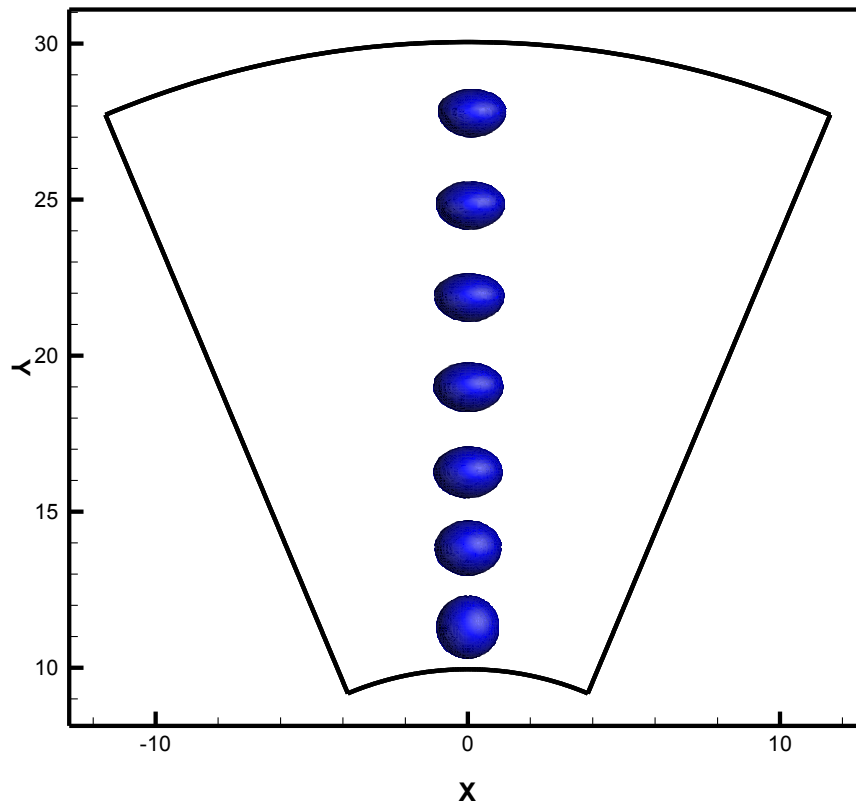


Figure 3. Time sequences of an air bubble rising in quiescent water.

C. Liquid Drop Impact onto a Liquid Pool

A water drop with a diameter of 2.9 mm impact onto a deep water pool is simulated. In this test, the experimental case with a falling height of 170 mm in Ref. 21 is simulated, where the corresponding $Fr = 85$, $We = 96$, and $Re = 4480$. The simulation conditions are the same as those used in Ref. 21. The simulations are performed on a $2D$ axisymmetric domain. Details of the computational setup can be found in Ref. 21. A fully $3D$ simulation was carried out in Ref. 2 on a Cartesian grid.

Time sequences of the drop impingement process along with the video images and simulations presented in Ref. 21 are shown in Fig. 4. The major events of the impact process, such as the formation of the vortex rings, entrapment of an air bubble during the cavity collapse and formation of the thin high speed liquid jet, are well captured in the current simulation. The predicted interface profiles also match both the experimental image and

simulations very well. Due to the neglect of the gas phase dynamics in the numerical model used in Ref. 21, the air bubble could not be captured in their simulations.

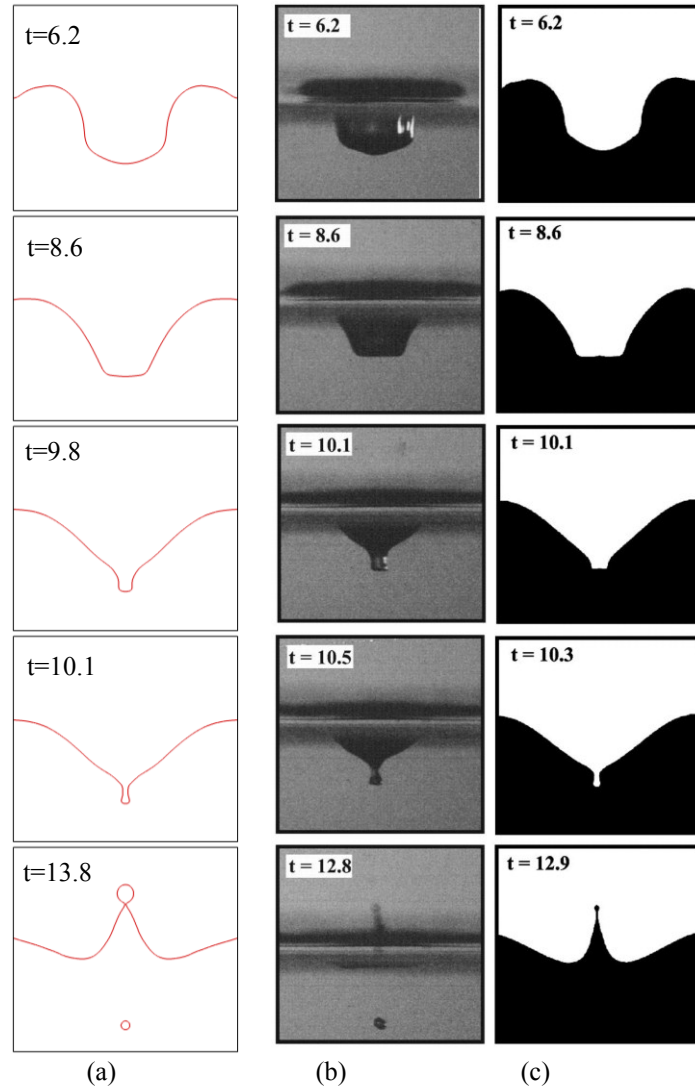


Figure 4. Time sequences of a water drop impact onto a deep water pool. (a) Present simulation; (b) experiment;²¹ (c) simulation.²¹

D. Wave Breaking by a Wedge-Shaped Bow

The geometry of the wedge, the computational domain are shown in Fig. 5. The geometry of the wedge is similar to the large wedge model used in Ref. 22. The side length of the wedge is $L = 0.75$ m, and the height of the wedge is $H = 1.0$ m. The half wedge angle is $\theta = 26^\circ$ and the flare angle $\varphi = 0^\circ$. The sharp edge corners are rounded with an arc of a small radius in order to make the grid orthogonal at the corners. The grids are refined near the solid surface.

In the case considered here, the water depth is $d = 0.0745$ m and the upstream velocity is $U = 2.5$ m/s, the corresponding Reynolds number, $Re = \rho U d / \mu$, is 1.64×10^5 , and the Froude number, $Fr = U / \sqrt{g d}$, is 2.93. The domain of the orthogonal curvilinear grid are $x = [-5.33 \text{ m}, 4.55 \text{ m}]$, $y = [-0.0745 \text{ m}, 0.6 \text{ m}]$, and $z = [0 \text{ m}, 5 \text{ m}]$ as shown in Fig. 5. Uniform inflow and convective outflow boundary conditions are used. Slip wall boundary conditions are imposed at all the other boundaries. A uniform velocity field same as the upstream velocity is prescribed to the entire computational domain at the $t = 0$.

Figure 6 shows the computed bow wave profile compared with the experimental video image. As shown in the figure, the overall structure of the wave is very similar to the experimental observation, such as the thin liquid sheet at the leading edge of the bow, overturning jet, jet plunging onto the free surface, and splashes at the wake. As the

liquid sheet overturns, the sheet is stretched and fingered up, and some "cylindrical drops" then pinch off from the liquid sheet, when the detached drops impact onto the water surface, a spray region is created.

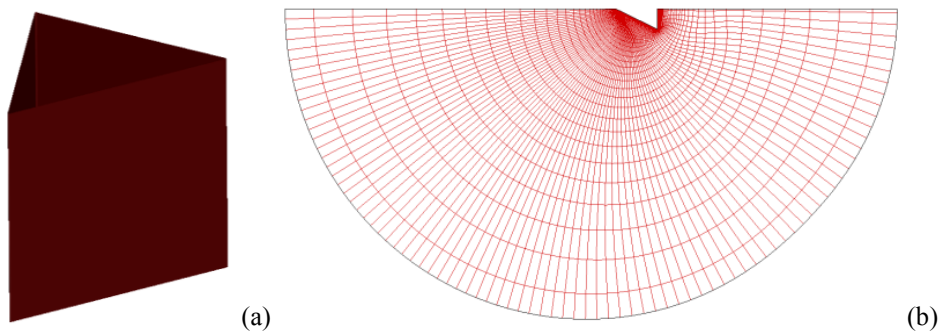


Figure 5. Wedge geometry and grid structure. (a). Wege; (b). Grid.

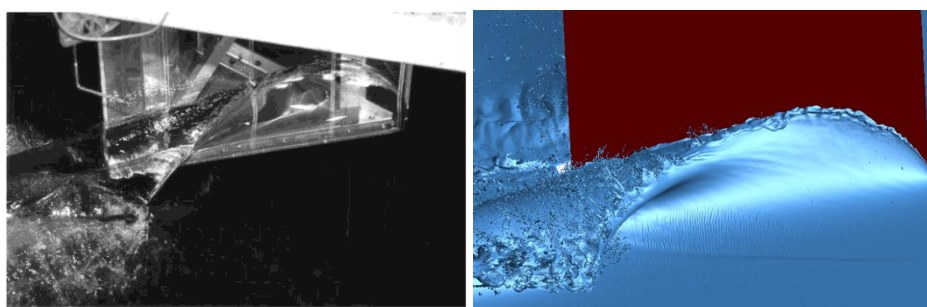


Figure 6. Wave profiles for both experiment (Ref. 22) and simulation with 1 billion grid points.

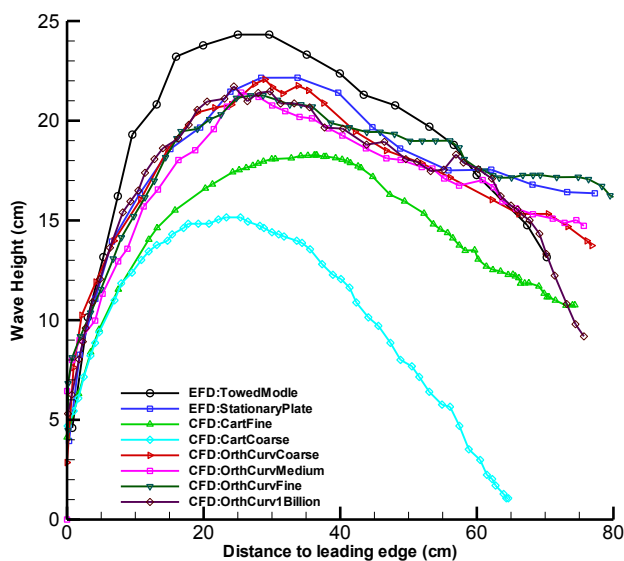


Figure 7. Comparison of the wave elevation with the experimental results (Ref. 22).

The wave contact line elevations along the wedge side starting from the leading edge for different cases compared with the experimental measurements are shown in Fig. 7. For comparison purposes, the computational results on the Cartesian grid are also presented in Fig. 7. Both the experimental results²² for the towing tank model and the flume model are included in the figure. As shown in the figure, the maximum height of the flume case is

below the towing tank case. It was explained that this discrepancy might be due to the camera orientations which might not be exactly perpendicular to the model and parallel with the undisturbed free surface.²³

The overall wave contact line profiles from both the simulations and experiment have the similar trend. For the coarse Cartesian grid, the wave height is far below the experimental results. With increased grid resolutions near the wall, the wave height increases significantly. Grid refinement near the solid wall is much easier for the curvilinear grid than the Cartesian grid. With the orthogonal curvilinear grid, the grid resolutions near the solid wall are further increased without substantial increase of the total grid points. The wave height computed on the orthogonal curvilinear grid is greatly increased, which is very close to the flume model case.²²

In the future work, the mechanism of the liquid sheet disturbance, spray formation including fingering structure and pinching off drops will be investigated. Finer grid (3 to 4 billion) will be used in order to effectively resolve the small-sized bubbles/drops in the plunging region. With the finer grid, bubbles/drops size, and distribution will be calculated and compared with the available experimental data.

IV. Conclusions

A sharp interface LES methodology on orthogonal curvilinear grid for breaking waves produced by an interface-piercing body at high Reynolds number is presented. The Cartesian grid solver developed in Ref. 1 is extended to orthogonal curvilinear coordinates for fully resolved boundary layer. Both gas and liquid phases are considered for the strong interactions between two phases, such as spray dispersion and bubble entrainment. The level-set based ghost fluid method is adopted for sharp interface treatment and a volume-of-fluid method in orthogonal curvilinear coordinates is coupled with the level set method for enhanced interface tracking properties. A Lagrangian dynamic Smagorinsky subgrid-scale model is used for the spatially filtered turbulence closure.

Several numerical tests are conducted in order to validate the code. The orthogonal curvilinear grid solver is first tested by the LES of a fully-developed turbulent channel flow, where only single phase flow is considered. The computational results are compared with the DNS data reported in literature and good agreement is obtained. As two challenging examples for two-phase interfacial flows, a small-scale air bubble rising in quiescent water and a liquid droplet impact onto a liquid pool are modeled. Both cases match the experimental observations and measurements very well. Finally, wave breaking around a wedge-shaped bow is simulated. The predicted overall bow wave profile including thin liquid sheet at the leading edge, overturning jet and plunging, and splashes at the wake are very similar to the experimental observations. With increased grid resolution near the side wall of the wedge using the orthogonal curvilinear grid, the maximum elevation of the wave crest increases dramatically which matches the flume model case very well.

In the future work, the numerical tests will be further validated and grid refinement study will be conducted for each test cases. More numerical tests and examples, such as Wigley hull, will be included in order further verify and validate the code.

Acknowledgments

This work was supported by research Grants N00014-01-1-0073 and N00014-06-1-0420 from the Office of Naval Research (ONR), with Dr Patrick Purtell as the program manager. The simulations presented in this paper were performed at the Department of Defense (DoD) Supercomputing Resource Centers (DSRCs) through the High Performance Computing Modernization Program (HPCMP).

References

¹Yang, J., Stern, F., "Sharp interface immersed-boundary/level-set method for wave-body interactions," *Journal of Computational Physics*, Vol. 228, 2009, pp. 6590-6616.

²Wang, Z., Yang, J., Koo, B., Stern, F., "A coupled level set and volume-of-fluid method for sharp interface simulation of plunging breaking waves," *International Journal of Multiphase Flow*, Vol. 35, 2009, pp. 227-246.

³Wang, Z., Yang, J., Stern, F., "URANS study of air-layer drag reduction in a high-Reynolds-number flat-plate turbulent boundary layer," *40th AIAA Fluid Dynamics Conference*, Chicago, Illinois, June 28-July 1, 2010, AIAA paper 2010-4276.

⁴Yang, J., Stern, F., "Efficient simulation of fully coupled wave-body interactions using a sharp interface immersed-boundary/level-set method," *ASME 2010 3rd Joint US-European Fluids Engineering Summer Meeting*, Montreal, Canada, August 2-4, 2010, FEDSM-ICNMM2010-30103.

⁵Yang, J., Michael, T., Bhushan, S., Hanaoka, A., Wang, Z., and Stern, F., "Motion prediction using wall-resolved and wall-modeled approaches on a Cartesian grid," *28th Symposium on Naval Hydrodynamics*, Pasadena, California, September 12-17, 2010.

⁶Wang, Z., Yang, J., Stern, F., "Numerical simulations of wave breakings around a wedge-shaped bow," *28th Symposium on Naval Hydrodynamics*, Pasadena, California, September 12-17, 2010.

- ⁷Bhushan, S., Carrica, P., Yang, J., and Stern, F., “Scalability study and large grid computations for surface combatant using CFDShip-Iowa,” *International Journal of High Performance Computing Applications*, Vol. 25, 2011, pp. 466-487.
- ⁸Koo, B., Wang, Z., Yang, J., and Stern, F., “Impulsive Plunging Wave Breaking Downstream of a Bump in a Shallow Water Flume—Part II: Numerical Simulations,” *Journal of Fluids and Structures*, 2011, doi:10.1016/j.jfluidstructs.2011.10.011.
- ⁹Bhushan, S., Hanaoka, A., Yang, J., and Stern, F., “Wall-Layer Modeling for Cartesian Grid Solver Using an Overset Boundary Layer Orthogonal Curvilinear Grid,” *49th AIAA Aerospace Sciences Meeting and Exhibit*, Orlando, Florida, 4 - 7 January 2011.
- ¹⁰Choi, H. and Moin, P., “Effect of the computational time step on numerical solutions of turbulent flow,” *Journal of Computational Physics*, Vol. 113, 1994, pp. 1-4.
- ¹¹Jiang, G.-S. and Peng, D., “Weighted ENO Schemes for Hamilton-Jacobi Equations,” *SIAM J. Sci. Comp.*, Vol. 21, 2000, pp. 2126-2143.
- ¹²Falgout, R. D., Jones, J. E. and Yang, U. M. “The Design and Implementation of HYPRE, Library of Parallel High Performance Preconditioners,” *Numerical Solution of Partial Differential Equations on Parallel Computers*, A.M. Bruaset and A. Tveito, eds. Springer-Verlag. Vol. 51, 2006, pp. 267-294.
- ¹³Shu C.-W., Osher S., “Efficient implementation of essentially nonoscillatory shock-capturing schemes,” *Journal of Computational Physics*, Vol. 77, No. 2, 1988, 439-471.
- ¹⁴Peng, D., Merriman, B., Osher, S., Zhao, H., and Kang, M., “A PDE-based fast local level set method,” *Journal of Computational Physics*, Vol. 155, 1999, pp. 410-438.
- ¹⁵Suh, J., Yang, J., and Stern, F., “The effect of air-water interface on the vortex shedding from a vertical circular cylinder,” *Journal of Fluids and Structures*, Vol. 27, No. 1, 2011, pp. 1-22.
- ¹⁶Koo, B., Wang, Z., Yang, J., Kang, D., and Stern, F., “Impulsive Plunging Wave Breaking Downstream of a Bump in a Shallow Water Flume,” *ASME 2010 3rd Joint US-European Fluids Engineering Summer Meeting*, Montreal, Canada, August 2-4, 2010, FEDSM-ICNMM2010-30102.
- ¹⁷Moser, R. D., Kim, J. and Mansour, N. N., “Direct numerical simulation of turbulent channel flow up to $Re_\tau = 590$,” *Physics of Fluids*, Vol.11, 1999, pp. 943-945.
- ¹⁸Rizzetta, D. P., Visbal, M. R. and Blaisdell, G. A., “A time-implicit high-order compact differencing and filtering scheme for large-eddy simulation,” *International Journal of Numerical Methods in Fluids*, Vol. 42, 2003, pp. 665-693.
- ¹⁹Clift, R., Grace, J. R., and Webber, M. E., *Bubbles, drops, and particles*, Academic Press, New York, 1978, p.54.
- ²⁰Tomiya, A., Celata, G. P., Hosokawa, S., and Yoshida, S., “Terminal velocity of single bubbles in surface tension force dominant regime,” *International Journal of Multiphase Flow*, Vol. 28, 2002, pp. 1497-1519.
- ²¹Morton, D., Rudman, M., Liow, J.-L., “An investigation of the flow regimes resulting from splashing drops,” *Physics of Fluids*, Vol. 12, 2000, pp. 747-763.
- ²²Waniewski, T.A., Brennen, C.E., and Raichlen, F., “Bow wave dynamics,” *Journal of Ship Research*, Vol. 46, 2002, pp. 1–15.
- ²³Waniewski, T., “Air entrainment by bow waves,” Ph.D. Dissertation, California Institute of Technology, Pasadena, California, 1999.